Engineering Structures 307 (2024) 117926

Contents lists available at ScienceDirect

Engineering Structures

journal homepage: www.elsevier.com/locate/engstruct

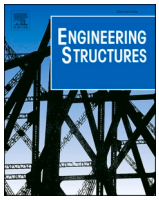

On the progressive collapse performance of RC frame structures under impact column removal

Fan Yi [a], Wei-Jian Yi [a,*], Jing-Ming Sun [a], Jia Ni [a], Qing-Feng He [a,b], Yun Zhou [a,b,c]

[a] College of Civil Engineering, Hunan University, Changsha 410082, China
[b] Key Laboratory for Damage Diagnosis of Engineering Structures of Hunan Province, College of Civil Engineering, Hunan University, Changsha 410082, China
[c] Key Laboratory of Building Safety and Energy Efficiency of the Ministry of Education, College of Civil Engineering, Hunan University, Changsha 410082, China

ARTICLE INFO

Keywords:
Progressive Collapse
Impact Loading
Event-dependent
Reinforced Concrete Frame Structures
Numerical Simulation

ABSTRACT

Currently, progressive collapse studies are mostly conducted based on an event-independent assumption. With studies employing an event-dependent premise mainly concerning explosion or fire events, the aftermath of impact loading is seldom reported. Meanwhile, interactions between reinforced concrete (RC) members and superstructures under impact loading need further evaluation. In this paper, finite element models of RC structures subjected to impact loading and progressive collapse are established and validated utilizing LS-DYNA. A valuing methodology of erosion parameters for the continuous surface cap model (CSCM) considering element size is proposed in this process. The influence of impact column removal (ICR) on the progressive collapse performance of RC frame structures is studied at sub-assemblage and structure levels. The parametric study indicates that the ICR process can be described by an impact loading stage and a gravity load stage. It is also found that structures experiencing ICR are exposed to a higher risk of progressive collapse, with the downward force exerted by the impacted columns being a significant contributing factor. Dynamic analyses demonstrate that the acceleration of the column removal point (CRP) can be used to validate and quantify the downward force. The hybrid force-displacement boundary conditions of frame columns give rise to the development of downward force. Recommendations for resisting progressive collapse considering ICR are proposed based on the analytical results of the paper.

1. Introduction

In recent two decades, progressive collapse studies of building structures, influenced by typical events like 9/11, have attracted extensive attention in the industrial and academic communities of structural engineering. Mechanisms resisting the progressive collapse of RC frame structures have been discussed by experimental [1,2], theoretical [3], and numerical studies [4,5]. Most existing studies employed the event-independent assumption [6], i.e., simulating extreme events by sudden column removal or nominal column removal (NCR). The event-independent assumption considerably reduces complexities and establishes the fundamental framework in the research field. Under this assumption, the structural robustness of target buildings can be scrutinised under critical conditions, where alternate paths for load transmission and unconventional load-bearing mechanisms, such as the compressive arch action (CAA) and catenary action (CA), are activated. Nonetheless, considering the increasing threat of terrorist attacks worldwide, further investigation into the influence of specific threats on the progressive collapse performance of building structures is beneficial for comprehensive evaluation of the safety and workability of building structures.

Some references suggest that the progressive collapse performance of structures could be adversely affected by extreme events. Shi et al. [7] argued that explosions not only cause failure of the target column but also simultaneously damage surrounding structural members. According to experimental data, Li et al. [8] suggested that fire-induced high temperature altered locations of plastic hinges and diminished their rotation capacity in RC joints. Fire-induced high temperature also impaired the residual load-bearing capacity and redistribution capacity of RC frames [9]. Further, Gombeda et al. [10] found out that the current state-of-the-practice design approach might not necessarily lead to conservative results against progressive collapse. It is also worth-noting that some studies focus on the influence of combined impact and blast loads on RC members [11,12]. It would be beneficial if relevant

* Corresponding author.
E-mail address: wjyi@hnu.edu.cn (W.-J. Yi).

https://doi.org/10.1016/j.engstruct.2024.117926
Received 4 September 2023; Received in revised form 20 March 2024; Accepted 23 March 2024

discussions and findings could be extended to research on the progressive collapse of structures. Before that, engineers need to obtain an understanding of progressive collapse behaviour subjected to individual threats, in which the impact loading still lacks focus.

Structural members could fail under vehicle or nearby building impact. According to a relevant study based on steel frames [13], overall damage of structures caused by impact is more severe than the ones subjected to NCR. It is perceivable that similar situations could happen to RC frames. Failure modes of RC frame columns under impact are different from existing progressive collapse studies employing NCR, so different consequences are expected. In the 1999 Kocaeli earthquake in Turkey, a corner column of an RC frame structure failed due to impact loading exerted by a collapsed adjacent building, as shown in Fig. 1 [14]. As illustrated, with the beam-column joint being intact, the bending process of column steel rebars could induce significant tensile force in the frame beams, which is apparently adverse for resisting progressive collapse.

Mechanics of impact dynamics [15] prove that the impact response of clamped and simply-supported members is discrepant, implying boundary conditions are decisive to the interaction between RC members and superstructures. In the field of crashworthiness, some studies employed the cantilever boundary condition for RC bridge piers [16–20]. Some other studies [21–23] concerning the influence of axial stress state applied constant axial load on the column top. These boundary conditions are based on two scenarios: the first one is the simply-supported bridge pier. The second one is the column in frame structures with minor post-impact deformation. However, the internal force distribution of frame structures is inevitably influenced by the support displacement since they are statically indeterminate, especially with significant geometric and material nonlinearity involved, which is common in progressive collapse studies.

Considering a single floor extracted from frames (Fig. 2). The static equilibrium state of substructure before column removal can be simplified as a single-degree-freedom model shown in Fig. 2c and Fig. 2f, where the upper and lower springs represent superstructures and the bottom column, respectively. When the bottom column is nominally removed (Fig. 2d), the column removal point (CRP) will rest in a new static equilibrium position Δ_{st}, if collapse is suppressed, as shown in Fig. 2g. If the CRP is subjected to downward forces (Fig. 2e), the point will exhibit additional vertical displacement Δ_{pf} (Fig. 2h). Therefore, if the displacement of the point after impact exceeds Δ_{st}, it indicates that the impact loading has induced downward forces. The load-bearing mechanism of structures can be summarised as a function $K_i = K_i(\Delta)$. Loads subjected to gravity within the affected area can be summarised as a mass point M_i of which the gravity load $M_i g$ is bear by $K_i\Delta_0$ and $K_C\Delta_0$, where K_C represents axial stiffness of the impacted column.

In progressive collapse, K_i is a nonlinear function that depends on both material and geometric characters. The dynamic equilibrium after the column removal, where the inertial and damping are involved, could be utilised to verify the downward forces, and the equation of motion is written as (Fig. 2h):

Fig. 1. Failed RC column due to impact of an adjacent building[14].

$$M_i\ddot{x} + c_i\dot{x} + K_i(x)x = M_i g + p(x) \tag{1}$$

where c_i is the damping coefficient, $p(x)$ is the external forces bearing on the CRP, e.g., the downward force. Based on Eq. 1, the effect of downward force on the acceleration of the CRP can be quantified, since the acceleration of the mass point is expressed as:

$$\ddot{x} = g - \frac{[(K_i(x)x + c_i\dot{x}) - p(x)]}{M_i} \tag{2}$$

for an isolated mass point in the gravity field, $c_i = 0, K_i(x) = 0, p(x) = 0$, so the second term of Eq. 2 equals zero, and it leads to the mass point undergoing free fall motion with gravitational acceleration; for a point of NCR, $c_i \geq 0, K_i(x) \geq 0, p(x) = 0$, so the second term of Eq. 2 is always a positive real value leading to an acceleration less than gravitational acceleration; for a point considering ICR, $p(x) > c_i + K_i(x)$, so the second term of Eq. 2 is a negative real value leading to an acceleration greater than gravitational acceleration. If the above three cases were to be plotted on one displacement history curve, then the curve of NCR and ICR would position opposing sides of a free fall curve.

In this paper, the ICR is studied to introduce a new event-dependent perspective of progressive collapse research, in which the finite element method (FEM) is adopted to conduct detailed investigations. In this process, the dynamic interaction between impacted columns and superstructures is investigated, and the downward force is found influential when considering ICR in progressive collapse analyses. A higher progressive collapse risk is identified for models implementing ICR compared with NCR because of the downward force. A new roadmap for research of frame members subjected to lateral impact loading is also indicated in this study considering their different boundary conditions compared to statically determined columns.

2. Model details and validations

Owing to high costs and difficulties, campaigns of large-scale tests face two challenging issues. Firstly, the number of specimens is often limited. Secondly, since the dynamic progressive collapse experiments are one-off, large-scale specimens usually are not loaded to collapse considering safety or loading capacity. As a result, data about collapse course from large-scale experiments is limited, especially the collapse load. FEM can address the above issues, provided that the authenticity and accuracy of models are thoroughly validated. For this purpose, a substructure experiment subjected to progressive collapse and a column experiment subjected to impact loading are validated in this paper, respectively. The value of erosion parameters considering the element size for concrete material was analysed hereby. Then, subsequent works were fulfilled on this base.

The naming rules of models in this paper are illustrated in Fig. 3, and they are composed of four items. The first item denotes the type of models, i.e., column (C), substructure (S), frame (F), and frame with boundary constraints (FBC). The second item denotes the column removal methods, which are static (S), nominal (N), and impact (I). The third item denotes the impact conditions of ICR, which are sorted as velocity, mass, and location, in which the units for the first two conditions are m/s and kg, respectively. Models without ICR are denoted with 'not applicable' (NA) on this item. The fourth item denotes the mass (ton) corresponding to loads that columns, substructures, or frames bear on a single floor.

2.1. Substructure models

Specimens from reference [24] are chosen for validation considering their successful implementations in validations [25,26]. In this reference, researchers constructed three identical single-floor substructures, in which one static (Con-1) and one dynamic (D-0.91) test are validated in this paper.

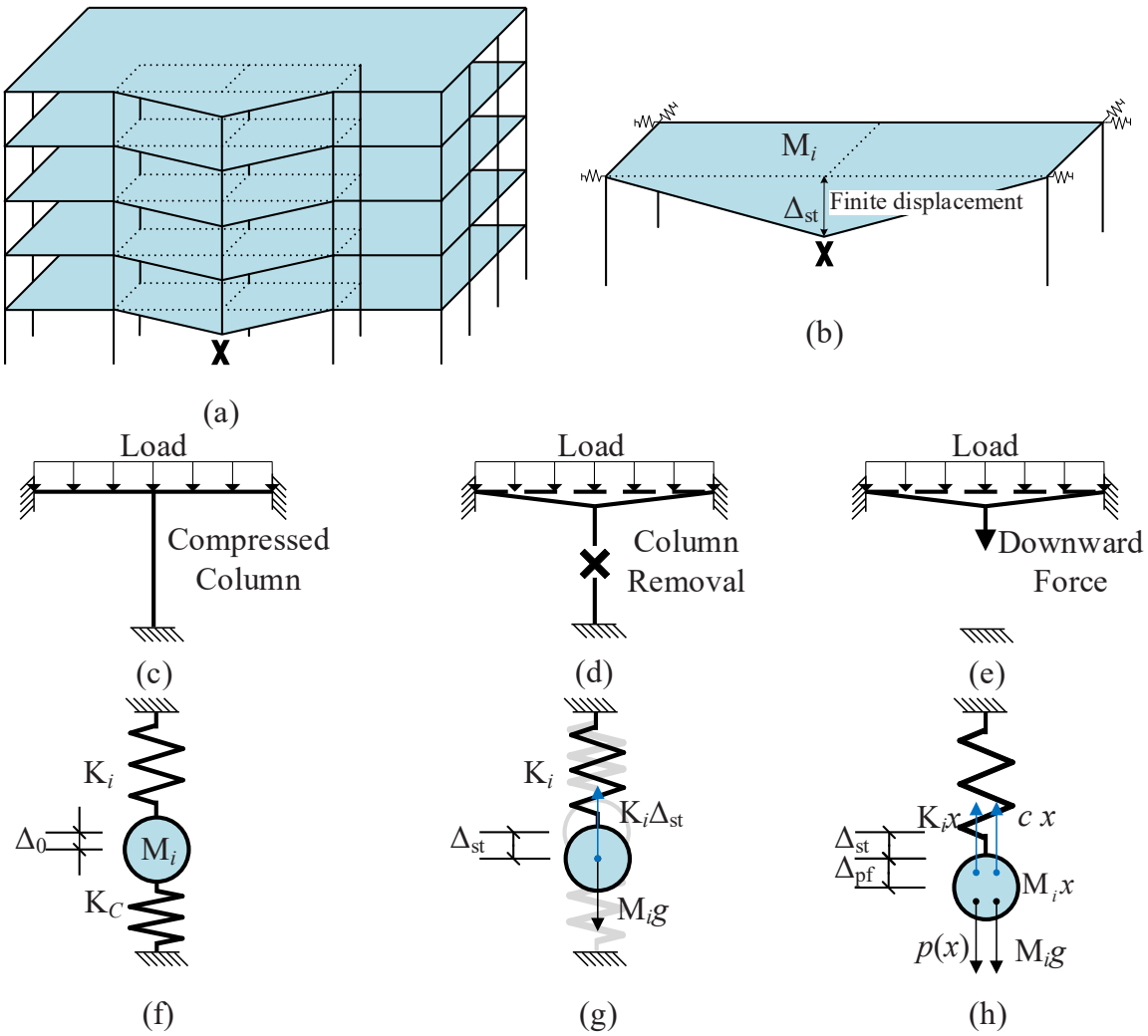

Fig. 2. Schematic of analytical models.

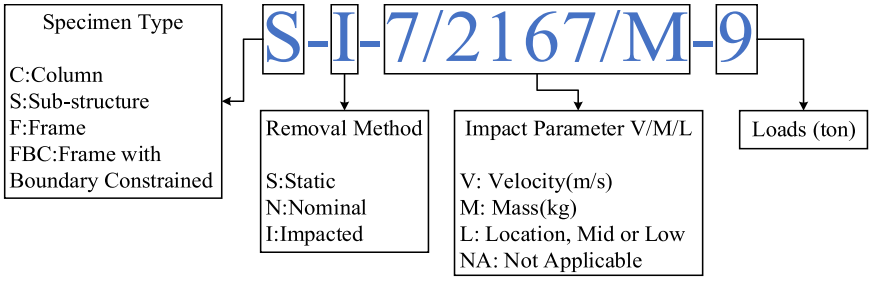

Fig. 3. Naming rules of models.

2.1.1. Specimen parameters

The finite element (FE) models employ two types of elements: the 2-node Hughes-Liu beam element with 2 × 2 Gauss quadrature integration, which simulates steel reinforcement, and the 8-node solid elements with reduced integration, which simulate solid objects. The reinforcement layout of the selected substructure and detailed data can be found in reference [24].

2.1.2. Material parameters

The continuous surface cap model (CSCM) was selected to model concrete. CSCM is a three-invariant model (I_1, J_2, J_3) practising the Willam-Warnke yield criterion. Continuous surface cap indicates the yield function accomplishes smooth transition by multiplying the shear yield surface and the hardening cap surface:

$$f\left(I_1, J_2, J_3, \kappa\right) = J_2 - \Re^2 F_f^2 F_C \tag{3}$$

where I_1, J_2, and J_3 are the first invariant of principle stress, the second invariant of deviatoric stress, and the third invariant of deviatoric stress, respectively. The inner state variable κ is the parameter that signifies cap hardening. F_f is the shear yield surface function; F_C is the hardening cap function; $\Re$ is the Rubin scaling function that determines the strength of concrete relative to uniaxial compression strength under arbitrary stress state.

CSCM is widely applied in studies concerning impact responses [12,27–31] and progressive collapse [32–35] of concrete structures. In terms of its parameter optimizations, Liu et al. [36] and Xu et al. [37] proposed modifications to the softening parameters and fracture energy parameters, respectively. Modifications proposed by Jiang et al. [38] on the Schwer_Murray_Cap model are also applicable to CSCM. Xu et al. [39] proposed modifications to the yield surface parameters and damage parameters facilitating its application for Ultra-High Performance Concrete (UHPC). Numerical simulations of progressive collapse often involve large deformations of elements, which could cause problems such as negative volume and exceedance of hourglass energy. Erosion algorithms can address these problems, but most studies have not quantitatively considered the influence of element size. The CSCM model concurrently employs the damage factor d and maximum principal strain as erosion criteria. When d approaches 1, elements have lost their strength and stiffness. Therefore, some scenarios with minor deformations might not require the application of erosion algorithm since the negative volume problem does not necessarily occur, as practised in some references [36,40], but progressive collapse apparently does not pertain to this category for the fact that excessive distortions in elements, which is the subsequent result of simulating large deformation of concrete members that typically occur due to the rotation at plastic hinge regions, will inevitably lead to negative volumes and trigger the calculation termination [7,25,33].

Fig. 4 compares the stress-strain curve of cylinder specimens in compression with an average element size of 25 mm under different erosion parameters ERODE. As shown in the figure, changing ERODE has a minor effect on the descending segments of the stress-strain curve. Under uniaxial compression, elements meeting the two erosion criteria were few, and damage contours of specimens with different ERODE are similar. The damage contour of the specimen with ERODE= 1.01, shown on the right side of Fig. 4, is selected to demonstrate the indicated failure mode. It can be observed that damaged elements distributed diagonally at a 45-degree angle, indicating a shear type failure that was documented in relevant testing standard [41] and reflecting the mechanical law that the direction of maximum shear stress is at a 45-degree angle to the direction of normal stress when specimens are subjected to uniaxial compression. Also, it is worth-noting that the shear failure is only one of the typical failure types for concrete cylinder specimens, of which failure types may vary depending on the height-to-diameter ratio, boundary conditions, or material compositions of specimens. Unlike uniaxial compression, concrete specimens only exhibit one transverse crack when subjected to uniaxial tension. The descending segment curve of tension specimens is therefore represented in terms of displacement or crack width [42]. Engineering practices indicate that when the crack width exceeds 0.4 mm, cracks traverse the section [43]. Therefore, this paper adopts a value of 0.4 mm as the critical crack width. As shown in Fig. 5, the elements would be infinitely stretched due to tension when ERODE= 0, which is unreal. With ERODE= 1.016, the deformation is 0.41 mm. For ERODE= 1.05 and 1.1, the deformations were 1.3 mm and 2.7 mm, respectively, significantly surpassing the deformations suggested by existing data.

Therefore, when ERODE is smaller than its minimum limit or when only the damage factor d is used as the erosion criterion (ERODE=1), elements may be prematurely removed, resulting in the model being overly brittle. The minimum limit for ERODE can be calculated as follows:

$$\mathrm{ERODE} = 1 + \frac{w_C}{l_e} \tag{4}$$

where, w_C is crack width under tension, and l_e is the characteristic length of elements. Still, considering the fact that reinforced concrete possesses more favourable crack control and ductility, its application on reinforced concrete members could be further investigated by incorporating calibrations on the constitutive models of concrete.

Simulations of dynamic tests employed a strain-rate effect algorithm based on viscoplasticity (IRATE=1) for CSCM, i.e., the viscoplasticity stress is calculated at each timestep by interpolating between elastic trial stress and inviscid stress. After being processed by the algorithm, the uniaxial compressive and tensile strength of concrete under dynamic conditions are as follows:

$$f_T'^{dynamic} = f'_T + E\dot{\varepsilon}\eta \tag{5}$$

$$f_C'^{dynamic} = f'_C + E\dot{\varepsilon}\eta \tag{6}$$

where $f_T'^{dynamic}$ and $f_C'^{dynamic}$ are dynamic tensile and dynamic compressive strength, respectively. f'_T and f'_C are static tensile and static compressive strength, respectively. E is Young's modulus, $\dot{\varepsilon}$ is the effective strain rate, and η is called fluidity coefficient. The strain-rate effect simulated by the viscoplasticity algorithm is greater under tension than under compression, which is consistent with experimental observations [44].

The density of concrete was 2500 kg/m^3, with measured compressive strengths of 23.0 MPa (Con) and 24.4 MPa (D-0.91) [24,25], respectively. The maximum aggregate size of the concrete was 19 mm. For dynamic tests, IRATE= 1 was chosen to activate the inbuilt strain-rate effect algorithm described in Eq. 5 and Eq. 6, which could lead to an increase in material strength in concrete elements when the strain rate is considerable. ERODE was set to 1.016 according to Eq. 4. Notably, in the subsequent validation of column tests, some parameters

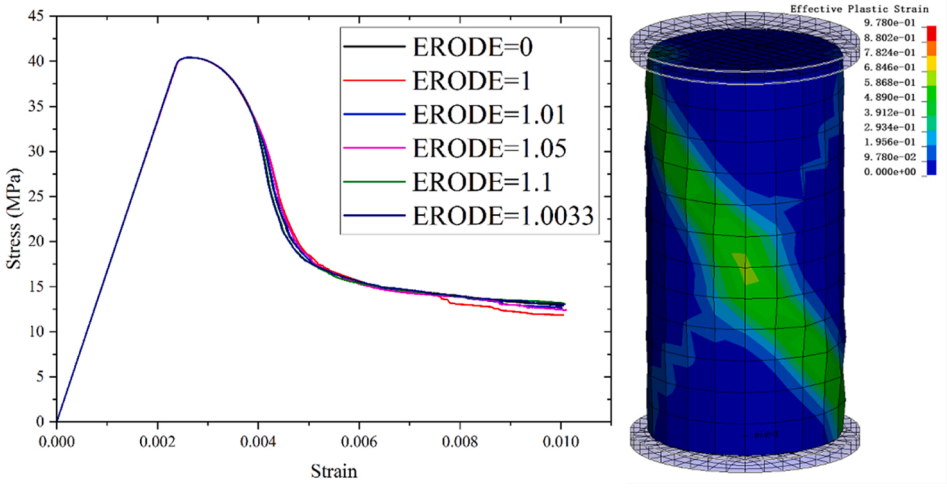

Fig. 4. Stress-strain curve and damage contour of CSCM models under uniaxial compression.

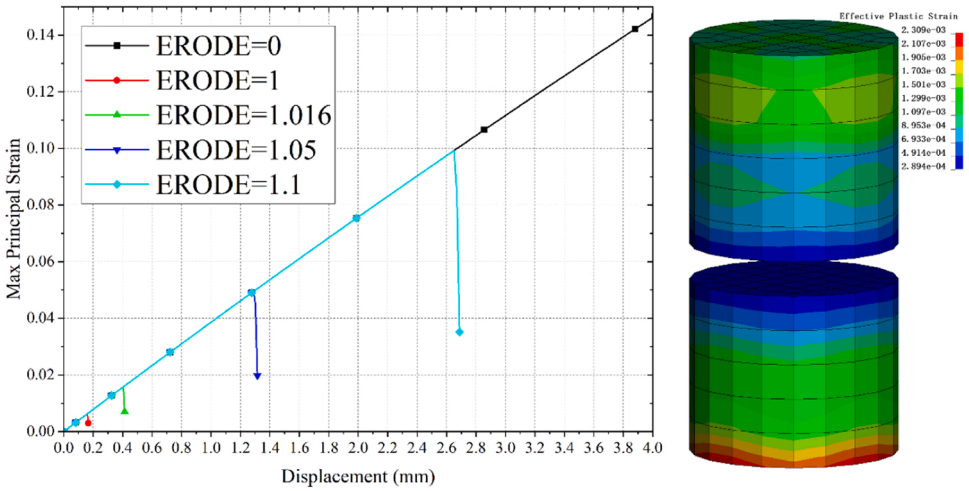

Fig. 5. Max principal strain vs. displacement curve and damage contour under uniaxial tension.

including the density and compressive strengths of concrete are varied.

The PIECEWISE_LINEAR_PLASTICITY was selected for steel reinforcement. Elastic modulus and tangent modulus were calculated accordingly [37]. In addition, the Cowper-Symonds equation was employed to account for the strain rate effect of steel reinforcement. The ratio of dynamic yield stress σ_0^d to static yield stress σ_0 is:

$$\frac{\sigma_0^d}{\sigma_0} = 1 + \left(\frac{\dot{\varepsilon}}{C}\right)^{1/P} \tag{7}$$

where the C and P are 0.04 ms^{-1} and 5 for low-carbon steel, respectively. In static tests, strain-rate effects were disregarded (IRATE=0; C=0, P = 0).

2.1.3. Miscellaneous parameters

The AUTOMATIC_SURFACE_TO_SURFACE (ASTS) contact was utilised to define the contact between mass weights and specimens. The Constrained_Beam_in_Solid (CBIS) coupling algorithm was used to accomplish the coupling between steel reinforcement and concrete.

In dynamic tests, external loads were applied using gravity loading. In the D-0.91 test, the mass of a single mass weight was 4500 kg. Additionally, steel plates were suspended on slab flanges to simulate the rotational constraint of perimeter slabs on the structure. The paper also simulated the 12-points redistribution system for static tests, where rotational hinges (Revolute joint) or ball joints (Spherical Joint) were established at the nodes of both the primary beam and secondary beams, as well as between secondary beams and triangular plates aiming to resemble the experimental conditions with most efforts. The static model is solved using the explicit solver, in which a prescribed vertical motion is applied to the element located at the midpoint of the primary beam to simulate the concentrated load applied by the hydraulic jack in the test. The prescribed vertical motion is realised by the BOUNDARY_MOTION_NODE keyword with a loading rate of 30 mm/s. This loading rate is considered pseudo-static because the differences in damage patterns and load-displacement curves of simulations with further decreased loading rates are negligible.

The sudden gravity field induces dynamic effects, addressed in this paper through the mass damping method for stress initialization. Specifically, in the first step, the mass damping coefficient was determined through eigenvalue analysis using the keywords Control_Implicit_Eigenvalue and Control_General. It is found that the mass damping coefficient calculated using the first order frequency meets the requirement of eliminating dynamic effects. The calculated mass damping coefficient is 0.006716, which is twice of first order frequency of substructures. The second step is determining the history curve for applying the mass damping coefficient. The method proposed in reference [45] was adopted to fulfil the gradual transition of global damping (Damping_Global).

According to the experiment [24], fixed supports were applied to 5 edge columns using Boundary_SPC_Set, and the effect of 'sudden column loss' was achieved using the Mat_Add_Erosion, as shown in Fig. 6.

2.1.4. Impact column removal models

By adding pendulum and column models, along with corresponding boundary conditions and contact relationships, substructure models subjected to ICR were established, as depicted in Fig. 7. The pendulum weighing 2167 kg was modelled with the Pendulum Test Facility at Hunan University as the reference [46]. The pendulum consists of the impactor cap and the impactor weight, in which the cylindrical cap is 520 mm in height and 200 mm in diameter. The impact surface was processed into a curved surface with an equivalent radius of 400 mm. The impact point was located at the middle of the column, where is 500 mm from the column bottom. Stress initialization was completed at 130 ms, and a 7 m/s velocity was imparted to the pendulum model. Material of the pendulum employs the RIGID constitutive model with parameters of low-carbon steel. The cross-sectional dimensions of the impacted column are 125 mm × 125 mm, with a height equal to adjacent columns. The impacted column was reinforced with 4T10 longitudinal rebars and stirrups of R3 @ 60, where T and R denote the surface geometry of rebars, for example, T10 stands for deformed rebars of 10 mm diameter, and R3 stands for plain round rebars of 3 mm diameter, in accordance with the referred studies [24]. The shared node method was utilised to connect the top of the impacted column and the substructure, with the bottom being fixed support. The ASS (AUTOMATIC_SINGLE_SURFACE) contact was established between the pendulum and the impacted column.

2.2. Column models

The column experiment from reference [21] is chosen for validation. The tested columns were hinged on one end with a translational constraint and pinned on a 20-ton mass weight sliding along the column axis on the other end, representing the inertia of superstructures. Four prestressed tendons passing through the reaction frame and the mass weight were utilised to apply axial compression, which are 197 kN and 201 kN for the SB2 and SB3 specimens that were validated in this paper, respectively. The cross-sectional dimensions of specimens are 300 mm × 300 mm, equipping 4T28 longitudinal rebars and T12 @ 150 stirrups. The mass of the impactor is 1140 kg, and other parameters are illustrated in Fig. 8 and Fig. 9.

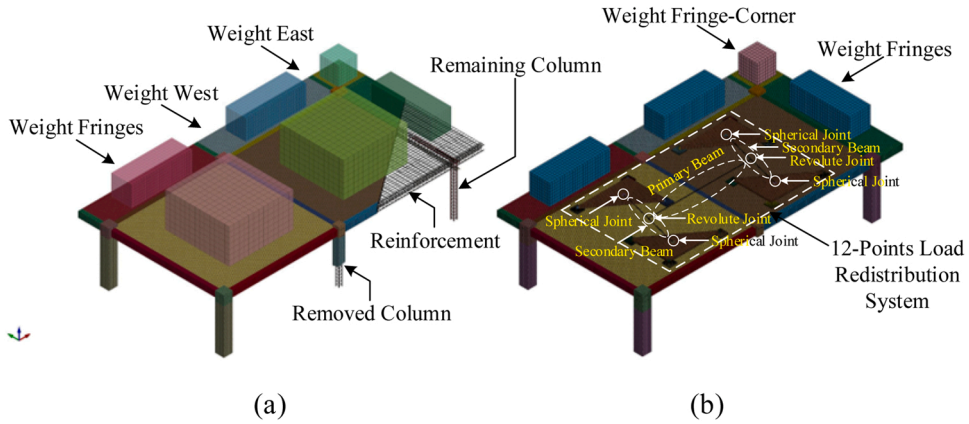

Fig. 6. Schematic of substructure models: (a) Dynamic model, (b) Static model.

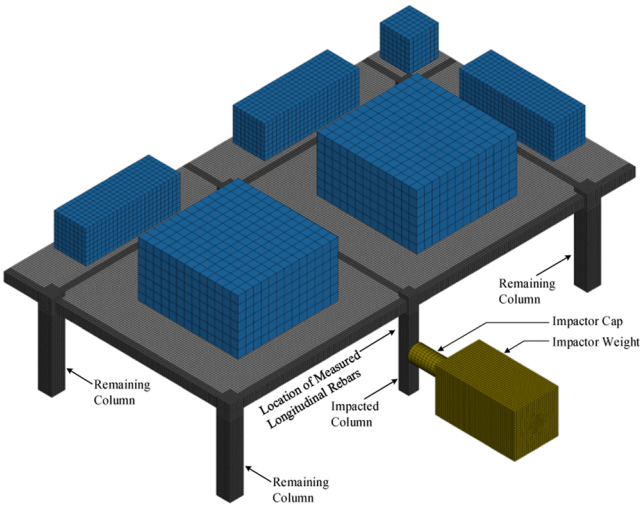

Fig. 7. Schematic of ICR substructure models.

2.2.1. Element and material parameters

An average mesh size of 20 mm was employed for concrete and reinforcement elements based on mesh sensitivity analyses. MAT159_CSCM was adopted as the concrete material, with a density of 2400 kg/m^3, uniaxial compression strength of 39.5 MPa, and a maximum aggregate size of 19 mm. The MAT024_PIECEWISE_LINEAR_PLASTICITY was adopted for the steel reinforcement material, with a density of 7830 kg/m^3 , elastic modulus of 2.06×10^5 MPa, Poisson's ratio of 0.3, and yield strengths of 523 MPa for longitudinal rebars and 507 MPa for stirrups, respectively. Sliding bearings, the mass weight, and the impactor were modelled with MAT020_RIGID, with material parameters identical to the steel reinforcement as their elastic deformation are not a consideration in this case.

2.2.2. Miscellaneous parameters

Rebar elements were also coupled with solid elements by CBIS. The contact between the impactor and the specimen employs ASS. Besides, all other contact relationships in the column models employ ASTS. In order to simulate the axially compressed state of columns in tests, the left end of the model columns was fixed on a rigid plate of which all DOFs were constrained by BOUNDARY_ SPC_SET. On the right end, the Y-direction translation of the mass weight was released. Axial compression was simulated by nodal forces applied on the mass weight by LOAD_NODE_SET.

2.3. Validation results

2.3.1. Substructures

It can be observed from Fig. 10 that the substructure model exhibits damage along with edges of the negative moment area of slabs, which is consistent with the damage pattern in the experiment on the crack distribution surrounding slab edges. Also, it can be observed that the FE model exhibits the torsion of beam 4–3/A and the fracture of

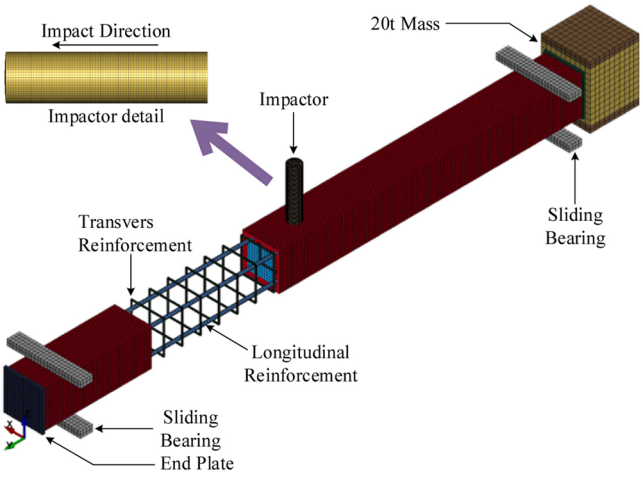

Fig. 9. Column impact models.

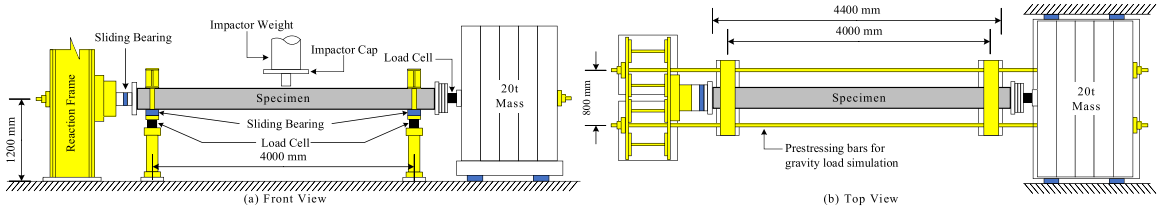

Fig. 8. Column impact test setup.

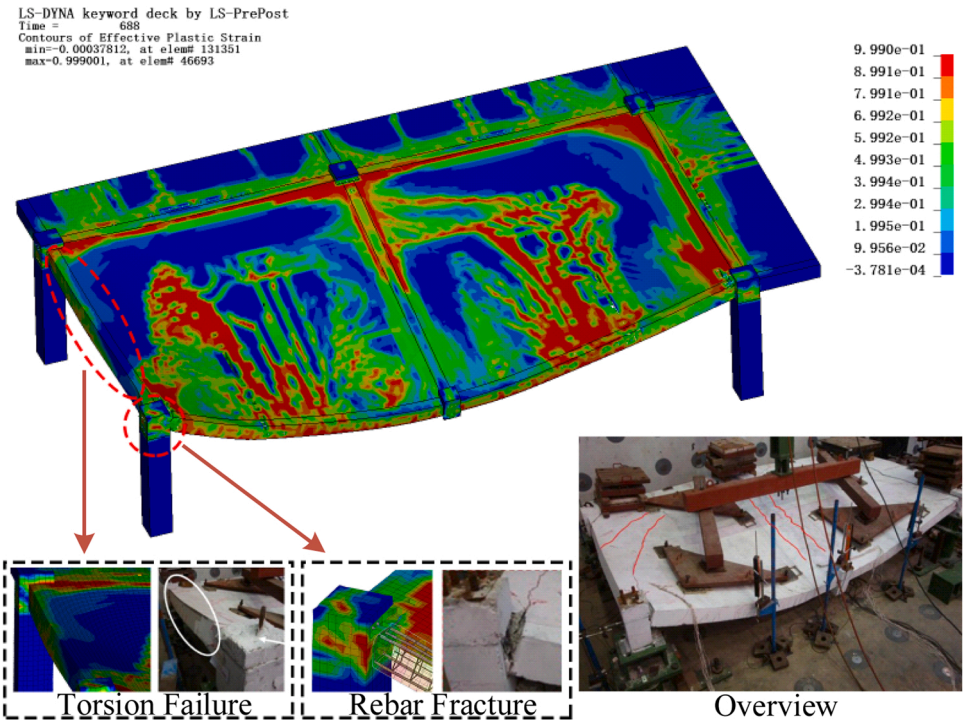

Fig. 10. Comparison of damage patterns in the static test (specimen Con-1 and model S-S-NA-NA).

longitudinal reinforcement of beam A-B/4. One deviation is that the slab damage in the FE model is more concentrated around edges. According to reference [47], this deviation could be ascribed to that the load distribution accomplished by the 12-points redistribution system cannot be accurately simulated. In the large deformation stage, more vertical loads are redistributed to points near perimeter beams, for connections between the primary beam and secondary beams are semi-rigid.

Fig. 11a illustrates the vertical displacement-force curve of the static test at CRP. The FE model can generally depict the force-displacement trend of the substructure under static loading. However, due to slightly lower stiffness and yield point values in the elastic stage compared to experimental results, the force in the plastic stage is slightly lower than the experimental values. Fig. 11b compares the vertical displacement history of the dynamic test from the experiment [24], a reference [26], and this study. It is shown that both FE results kept favourable consistency with the experimental result. In the experiment, the substructure achieved its peak displacement of 43 mm, and the residual displacement stabilised at 40 mm, while in the FE model of this study, the residual displacement was 38 mm.

Fig. 12 shows the slab crack distribution from the D-0.91 test [24], the FE result from reference [26], and the FE result from this study (S-I-7/2167/M-9). Both FE models captured the damage mode that cracks primarily propagate along the edges of the slab. The beam 4–3/B in the Y-direction plane exhibits greater damage compared to the other two beams connected to the removed column, A-B/4 and B-C/4, which are oriented in the X-direction plane. This is because beam 4–3/B becomes a cantilever after column removal, impairing the formation of the catenary action (CA).

2.3.2. *RC columns*

Fig. 13 compares the impact force and displacement history of the SB2 specimen (longitudinal rebar diameter = 25 mm, impact velocity = 3 m/s, corresponding to the C-I-3/1140/M-10 model) and the SB3 specimen (longitudinal rebar diameter = 28 mm, impact velocity = 4.5 m/s, corresponding to the C-I-4.5/1140/M-10 model). As shown in the figure, FE models exhibit a promising result of the peak impact force, while some discrepancies exist in the plateau stage for both SB2 and SB3. The two graphs also indicate a high degree of consistency in terms of displacement peaks. The SB2 specimen shows some differences in residual displacement compared to the experiment, as can be observed in Fig. 13a. Additionally, both specimens show a delayed occurrence of displacement peaks compared to the impact force peaks, suggesting the existence of inertial effects.

3. Substructures under ICR

Table 1 presents all the models established for analysis in this study, with impact parameters like impact velocity, pendulum mass, and impact location tabulated within. In these models, Models 1 to 4 are established for validation based on SB2 and SB3 specimens of reference

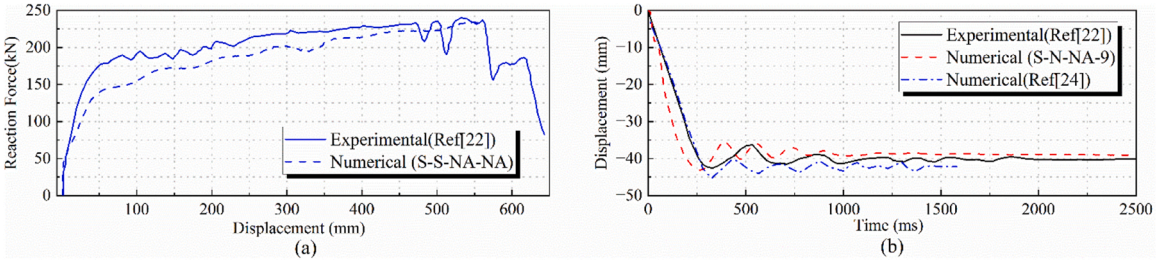

Fig. 11. Comparison of displacement curves: (a) static, (b) dynamic.

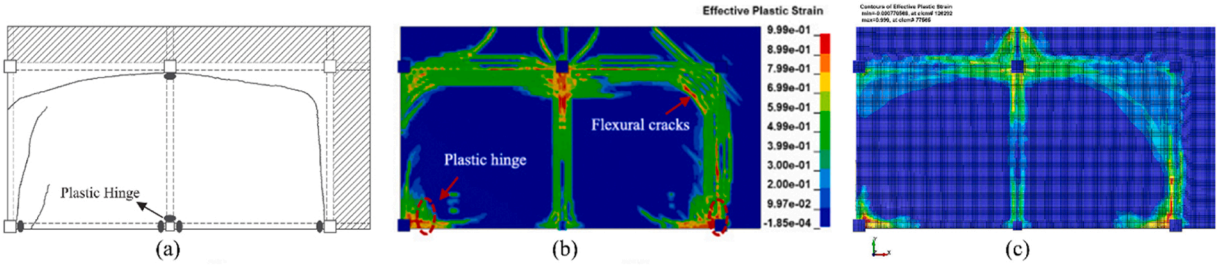

Fig. 12. Comparison of top views in the dynamic test: (a) experiment, (b) reference[26], (c) this paper.

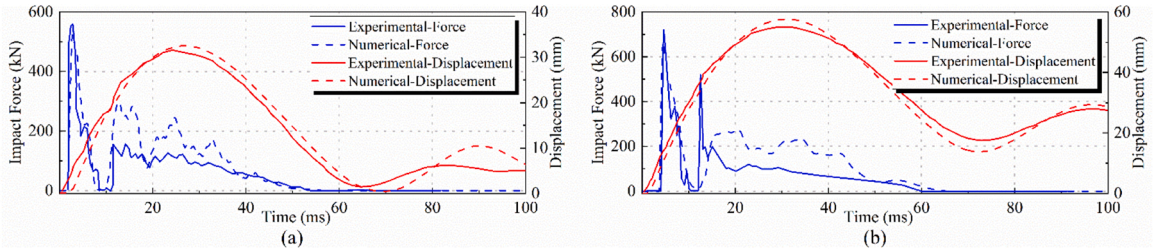

Fig. 13. Comparison of the column model validation: (a) SB2, (b) SB3.

[21], and Con and D-0.91 specimens of reference [24]. Models 5 to 13 are substructure models in Section 3 mostly used for the parametric study. Model 4 employing NCR is also utilised hereby for comparing progressive collapse performance with ICR (Model 5). Models 14 to 21 are frame models for Section 4, including models based on the referred study and models exclude the influence of lateral stiffness.

3.1. Damage conditions

Fig. 14 compares the overall damage conditions of substructures under different removal approaches. It can be observed that the concrete damage on the slab top under ICR is significantly more severe than under NCR. Not only is the damage more severe in the slab's negative moment area and at the beam-column joints but also damage is evident within the semi-circular area surrounding the CRP. The damage on the slab bottom exhibits a trend radiating outward from the CRP to the peripheral area, in addition to a circular damage area appearing on the slab bottom in the ICR scenario.

Concrete damage under ICR is primarily composed by two parts. One part is similar to the NCR, and the other part is a circular damage area around the CRP induced by ICR. Fig. 15 depicts the top view of the damage contour of the S-I-7/2167/M-9 at typical moments. It can be seen that the circular initial damage on slabs propagates from the CRP to peripheral areas. A large area of damage appeared at the central area of slabs, while damage on beams and beam-column joint areas was comparatively slight. When the impact process came to its end, some damage also occurred on the far-end beam-column joint of the two-span beam directly attached to the impacted column. It can be inferred that the circular initial damage is a result of ICR. In the second stage, there is no significant change in the circular initial damage, while the damage in the beam and beam-column joint areas, which closely resembles that observed under NCR and corresponds to damage caused by the gravity load, continues to develop.

The damage condition of the impacted column is also observed.

Table 1
Model list.

No.	Name	Scale	Removal	Velocity (m/s)	Mass (kg)	Elevation	Weight (ton)
1	C-I-3/1140/M-10	Column	Impact	3	1140	Mid	/
2	C-I-4.5/1140/M-10	Column	Impact	4.5	1140	Mid	/
3	S-S-NA-NA	Sub-structure	Nominal	/	/	/	/
4	S-N-NA-9	Sub-structure	Nominal	/	/	/	9
5	S-I-7/2167/M-9	Sub-structure	Impact	7	2167	Mid	9
6	S-I-3/11798/M-9	Sub-structure	Impact	3	11798	Mid	9
7	S-I-5/4080/M-9	Sub-structure	Impact	5	4080	Mid	9
8	S-I-9/1310/M-9	Sub-structure	Impact	9	1310	Mid	9
9	S-I-7/2167/L-9	Sub-structure	Impact	7	2167	Low	9
10	S-N-NA-13.5	Sub-structure	Nominal	/	/	/	13.5
11	S-N-NA-22.5	Sub-structure	Nominal	/	/	/	22.5
12	S-I-7/2167/M-13.5	Sub-structure	Impact	7	2167	Mid	13.5
13	S-I-7/2167/M-22.5	Sub-structure	Impact	7	2167	Mid	22.5
14	F-N-NA-72	Frame	Nominal	/	/	/	72
15	F-I-10/2167/M-72	Frame	Impact	10	2167	Mid	72
16	F-N-NA-88.2	Frame	Nominal	/	/	/	88.2
17	F-I-10/2167/M-88.2	Frame	Impact	10	2167	Mid	88.2
18	FBC-N-NA-72	Frame w/ BC	Nominal	/	/	/	72
19	FBC-I-10/2167/M-72	Frame w/ BC	Impact	10	2167	Mid	72
20	FBC-N-NA-98	Frame w/ BC	Nominal	/	/	/	98
21	FBC-I-10/2167/M − 98	Frame w/ BC	Impact	10	2167	Mid	98

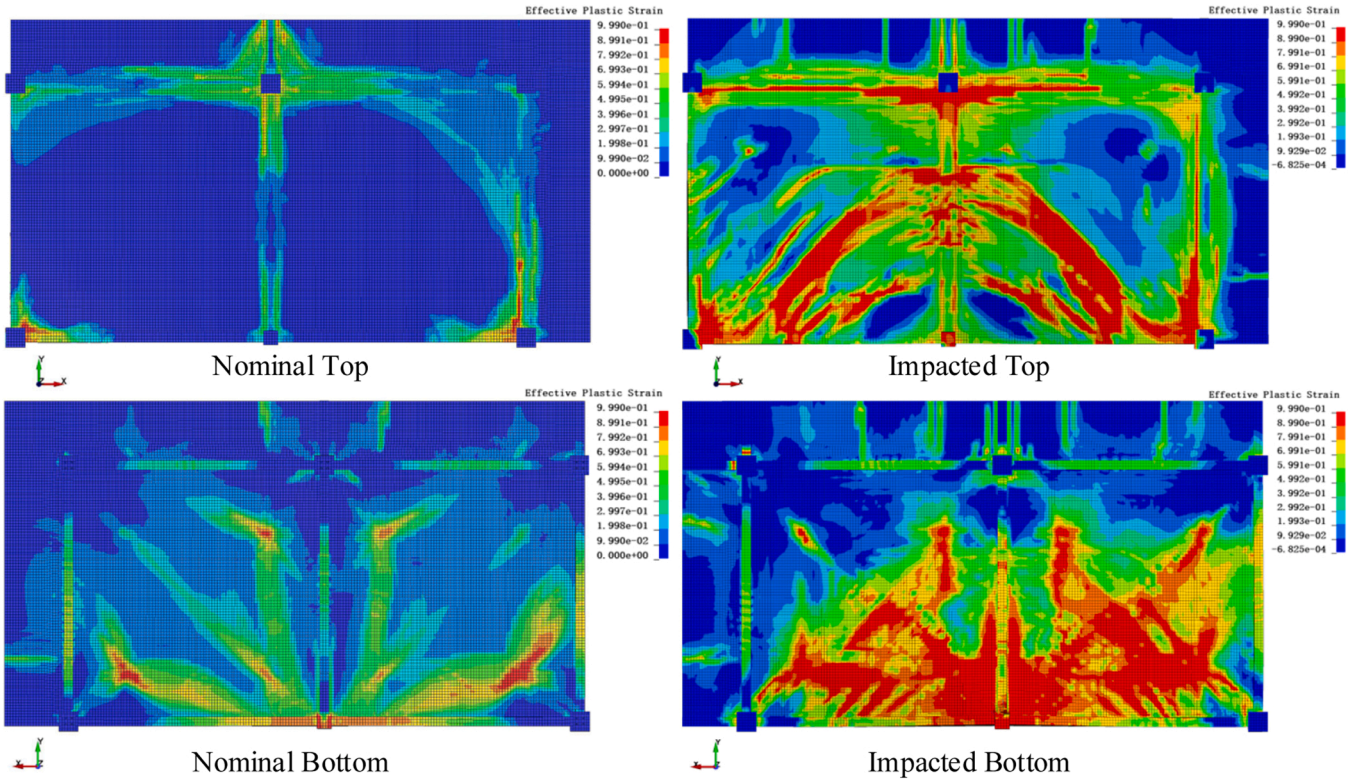

Fig. 14. Comparison of overall damage between NCR (S-N-NA-9) and ICR (S-I-2167/7/M-9).

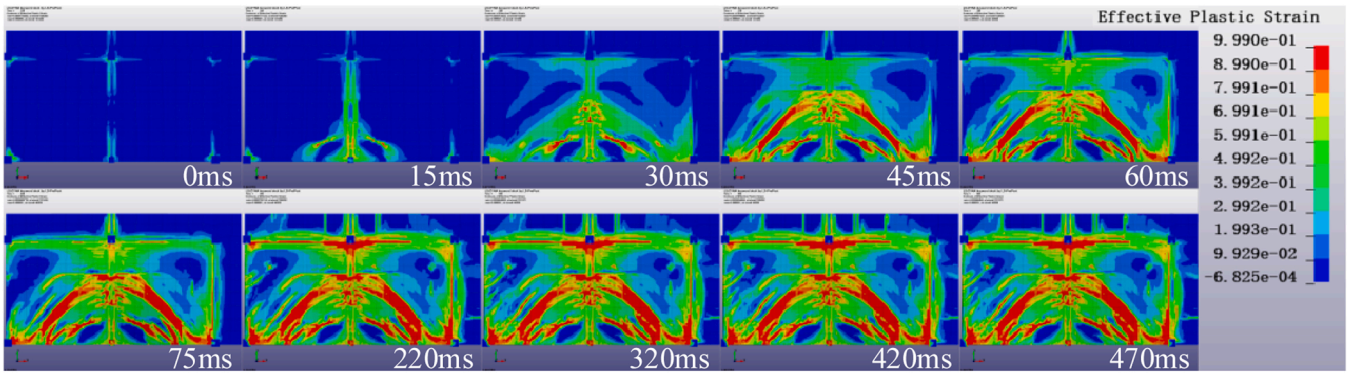

Fig. 15. Damage contour top view history of ICR (S-I-2167/7/M-9).

Fig. 16 displays typical moments of the column in the S-I-7/2167/M-9 model. After the impact commenced at 0 ms, surface damage appeared along the upper, lower ends, and the tensile side of the impacted column, indicating the occurrence of flexural damage in these regions. At 8 ms after contact, concrete elements erosion commenced at the upper end of the impacted column, accompanied by fractures of stirrups, suggesting the shear resistance of the column had been diminished. At 12 ms, the two longitudinal rebars near the pendulum fractured at the lower end, causing the lower part of the column to rotate and elongate around the remaining longitudinal rebars. During the 20 to 34 ms, the

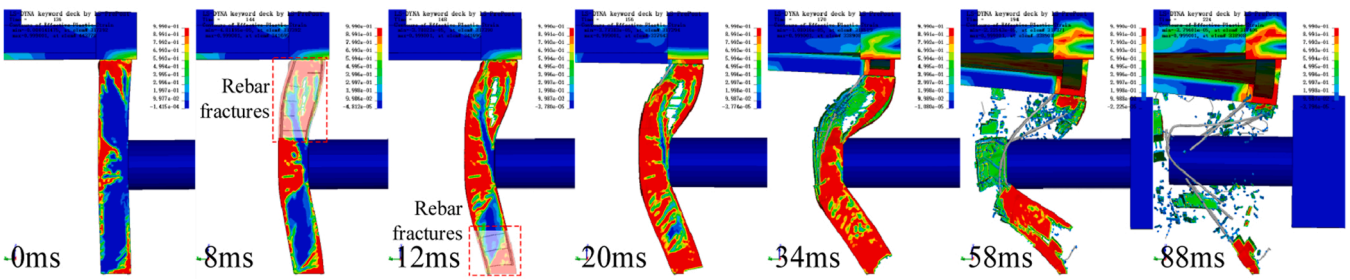

Fig. 16. Failure process of the impacted column (S-I-2167/7/M-9).

onset of vertical displacement at the CRP became observable. At 58 ms, the concrete elements exhibited a complete cross-sectional fracture. At 88 ms, the longitudinal rebars on the far side from the pendulum had fractured at the impact point. Combined with Fig. 15, it can be noticed that the division of the two stages in progressive collapse is roughly determined at 75 ms, which is close to the time when complete fracture of longitudinal rebars happened. Therefore, it can be concluded that the process of impact influences the progressive collapse of the substructure.

3.2. Displacement

The vertical displacement history for NCR, ICR and a free fall mass point are compared in Fig. 17a. As shown in the diagram, the time required to reach the peak is significantly shorter in the ICR scenario, with a residual displacement reaching 200 mm. While in the NCR scenario, the residual displacement is only 39 mm. At the initial few milliseconds after impact, the displacement of the CRP exhibited a short period of increase, peaking at 3.6 mm, followed by a rapid decline. This phenomenon at the early stage of ICR could be explained by a mechanism similar to compressive arch action (CAA). Importantly, the displacement curve of ICR lies below the one of free fall, indicating the presence of external loads beyond gravity and structural resistance during the column removal process.

3.3. Rebar strains

Fig. 17b illustrates the stress history average of the upper and lower longitudinal rebars symmetrically positioned on either side of the CRP. It is shown that the lower rebars of beams in both models were in compression before column removal. After the column removed, the lower rebars of the beam in NCR came to tensile, with the peak at 400 MPa and stabilizing at 350 MPa. In the case of ICR, corresponding rebars exhibited significant fluctuance and tension-compression transformations. The tensile strain attained its peak of 480 MPa at 33 ms, then turned to − 450 MPa and fluctuated drastically. Following column removal, the upper rebars in NCR shifted into compression, whereas in the ICR, the upper rebars rapidly transitioned from a compressive stress peak of 233 MPa to a tensile stress peak of 500 MPa, then maintained around 350 MPa. The two-span beams of the two substructures were at different resistance stages. In the NCR model, concrete damage concentrated at the lower part of the beam adjacent to the CRP and the upper parts of the beam-column joints at both side ends, exhibiting a typical CAA. In contrast, the concrete in the ICR model shows full-section damage, indicating the presence of a CA stage. Further, the time duration in CAA of ICR is short, which could be attributed to the downward force induced by impact loading. The CAA is a metastable state that the snap-through effect exists, so the short-duration-high-magnitude feature of the downward force could cause the two-span beam to cross over the peak of resistance provided by the CAA.

3.4. Downward force history

The strain of four longitudinal rebars on the top end of the impacted column in S-I-7/2167/M-9 are extracted and transferred into axial force, as shown in Fig. 18. In this figure, negative values denote compressive force, while positive values denote tensile force. The resultant force reached peaks of 129 kN, 20 ms after the impact initiation, coinciding with the time at which the outer longitudinal rebars reach their peak. At 46 ms, the outer longitudinal rebars fractured. Meanwhile, the tensile force in the inner longitudinal rebars increases rapidly, reaching its peak and coinciding with the second peak of the resultant force at 79.2 kN. By 72 ms, the inner longitudinal rebars also fractured, resulting in a swift reduction of stress in the longitudinal rebars.

The analysis above indicates that the downward force is provided by longitudinal rebars of the impacted column. Once all tensile longitudinal rebars fracture, the impacted column no longer exerts a downward force on superstructures. During the stage with the downward force, the acceleration at the CRP exceeds the gravitational acceleration. The downward force is characterised by high magnitude, with peaks several times the compressive force of the column. Fig. 14 and Fig. 15 demonstrate that downward forces lead to significant concrete damage in the substructure.

3.5. Parametric study

The parametric study is performed by incorporating variables such as mass-velocity combinations under constant kinematic energy, impact locations, and gravity loads, as illustrated in Fig. 19. It needs to be emphasised that conversions of physical quantities based on the similarity theory are conducted between the model and prototype when designing impact conditions of models, in which the impact mass and the velocity are determined considering specific requirements in relevant design codes [48,49]. In this study, the mass similarity constant and the time similarity constant are 1/3 and unity, respectively, leading to the derived velocity similarity constant of 1/3. The mass-velocity

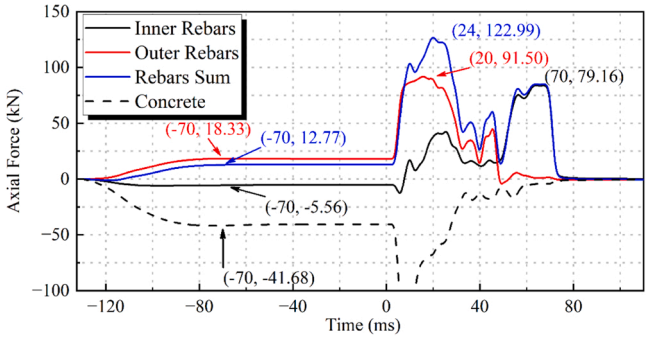

Fig. 18. Axial force history of longitudinal rebars in the impacted column of S-I-7/2167/M-9.

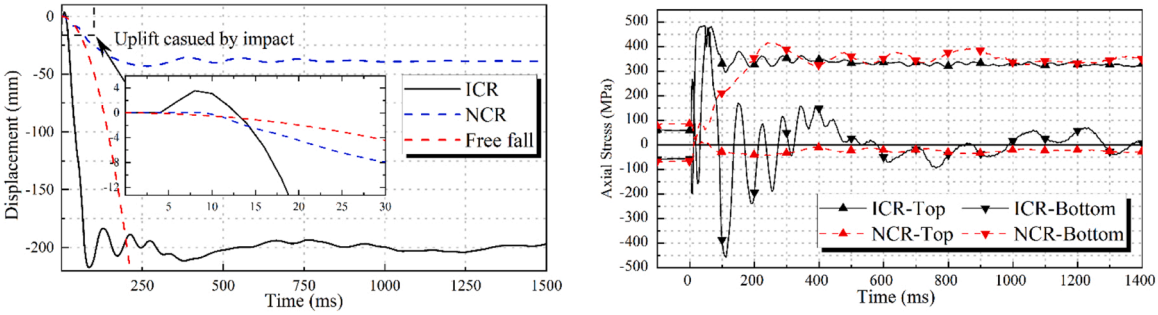

Fig. 17. Comparison between NCR and ICR: (a) Vertical displacement, (b) Longitudinal rebar strains.

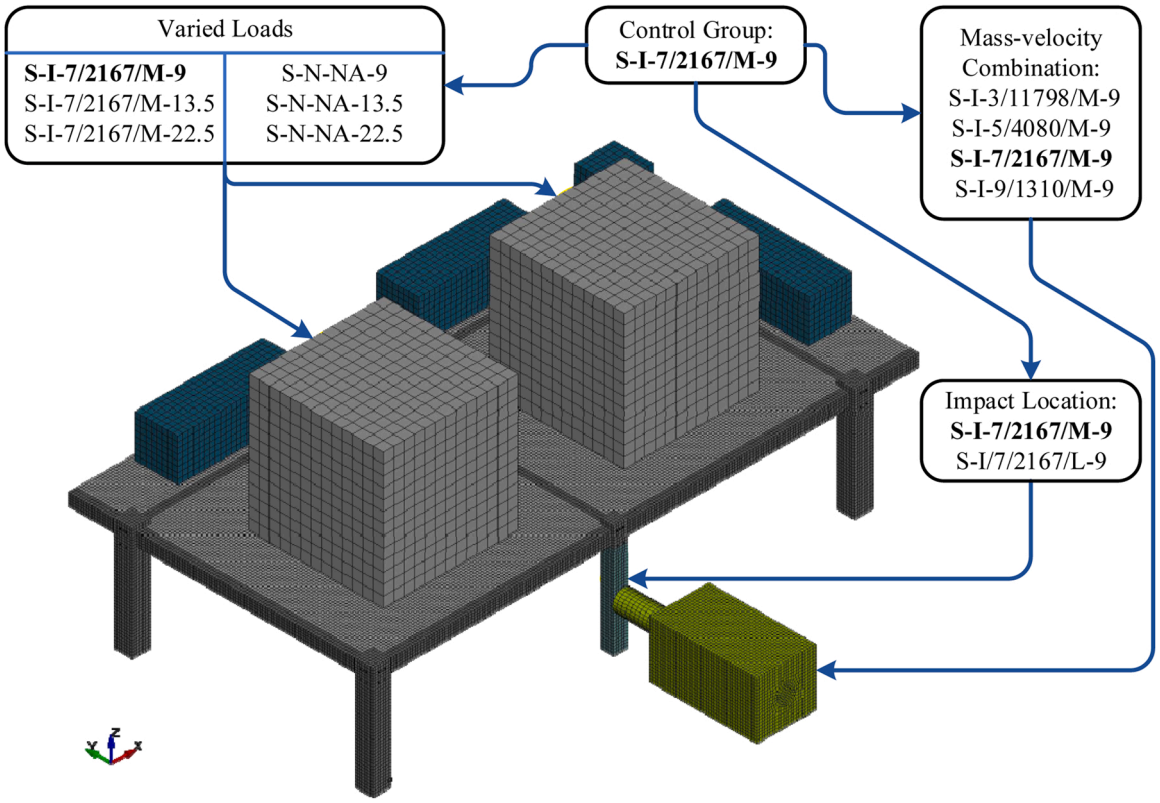

Fig. 19. Schematic diagram of varied parameters.

combinations are shown in Table 1 and Fig. 19. Two impact locations were modelled, including one in the middle of column (S-I-7/2167/M-9) and one near column bottom (S-I-7/2167/L-9). The load varied from 1 time (S-I-7/2167/M-9), 1.5 times (S-I-7/2167/M-13.5), and 2.5 times (S-I-7/2167/M-22.5) of the basic loads, in which the basic loads are 9 tons of mass wights.

As depicted in Fig. 20a, the curve of vertical displacement under different mass-velocity combinations all lies below the curve of free fall mass point after the initial uplift phase, indicating that all CRPs are influenced by external forces. Further, the vertical displacement exhibits a direct correlation with the increase of pendulum velocity, indicating an increasing impact velocity amplifies the conspicuousness of the downward force on the superstructures. However, the time is earlier when longitudinal rebars fracture near the bottom of the column. As a result, the residual displacement at the CRP will be relatively small like observed in S-I-5/4080/M-9.

Fig. 20c compares the curve of vertical displacement under different gravity loads. It can be observed that the curve is mainly comprised by two stages, of which the displacement in the first stage soon summits under impact loading in which the level of gravity loads has limited influence, and the second stage evolves under gravity loads. Under equal gravity loads, NCR models take longer to reach peak displacement than ICR models. Furthermore, the residual displacement of ICR models is significantly greater than those of NCR models, and a progressive collapse occurred in the case of S-I-7/2167/M-22.5, as shown in Fig. 22. The above comparison demonstrates that, with higher gravity loads, the structural resistance against progressive collapse subjected to ICR is relatively lower, and the NCR analysis leads to unsafety results.

The downward force history and downward force impulse history of substructures are demonstrated in Fig. 21. The duration of downward force ends when the vertical displacement reaches its first peak, indicating the conclusion of the impact loading stage. The impulse, as shown in Eq. 8, is derived by integrating the downward force over this period:

$$I_{\mathrm{df}} = \int_{t_0}^{t_{\mathrm{p1}}} F(t)_{\mathrm{df}}\,\mathrm{d}t \tag{8}$$

where $F(t)_{\mathrm{df}}$ represents the time-varying downward force, t_0 denotes the moment when impact commences, t_{p1} denotes the moment when the impact loading stage ends, I_{df} is the final impulse of downward force.

To facilitate comparison, curves are classified into two categories, in which one compares the mass-velocity groups with the control group (Fig. 21a and c), while the other compares the rest experimental groups with the control group (Fig. 21b and d). It can be observed from Fig. 21a that, the appearance of downward force peaks generally postpones with the decrease of impact velocity and increase of impact mass, and the peak value is around 100 kN, while no significant pattern between the mass-velocity combinations and peaks is found since the peak could appear around 20 ms or 60 ms, depending on specific failure scenarios of the impacted column. Also, the shape pattern of downward force curves is related to specific failure scenarios, in which, in more cases, the shape of downward force curves features with a two-peaks shape corresponding to the fractures of column longitudinal rebars near and far from the impacted face. Nevertheless, this shape pattern is relatively inapparent on S-I-3/11798/M-9, S-I-5/4080/M-9, and S-I-7/2167/L-9 because the two-peaks feature is eclipsed by a plateau duration with fairly high downward force. From both downward force curves, it can be observed that the peak will probably appear within the first 20 ms if the velocity is greater than 7 m/s. One exception is the S-I-7/2167/L-9 model, for which it indicates the impact location could influence the appearance of downward force peak measured on the column top. Further, the duration of downward force in most models is less than 80 ms, indicating the short period of the impact loading stage, except S-I-3/11798/M-9 which lasts for 150 ms.

The impulse history curves, on the other hand, demonstrate a more stable trend. It can be observed from Fig. 21c that, except the S-I-3/11798/M-9, rest models with varying mass-velocity combinations

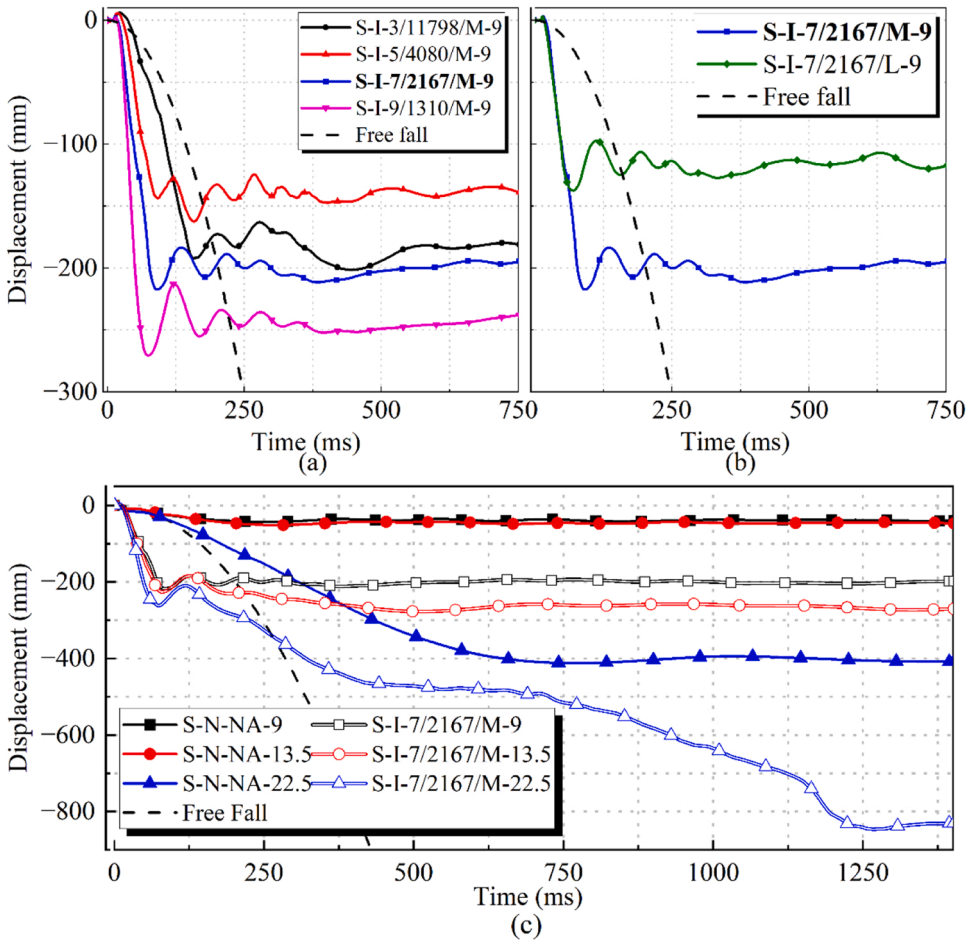

Fig. 20. Displacement history in parametric study: (a) Mass-Velocity, (b) Locations, (c) Loads.

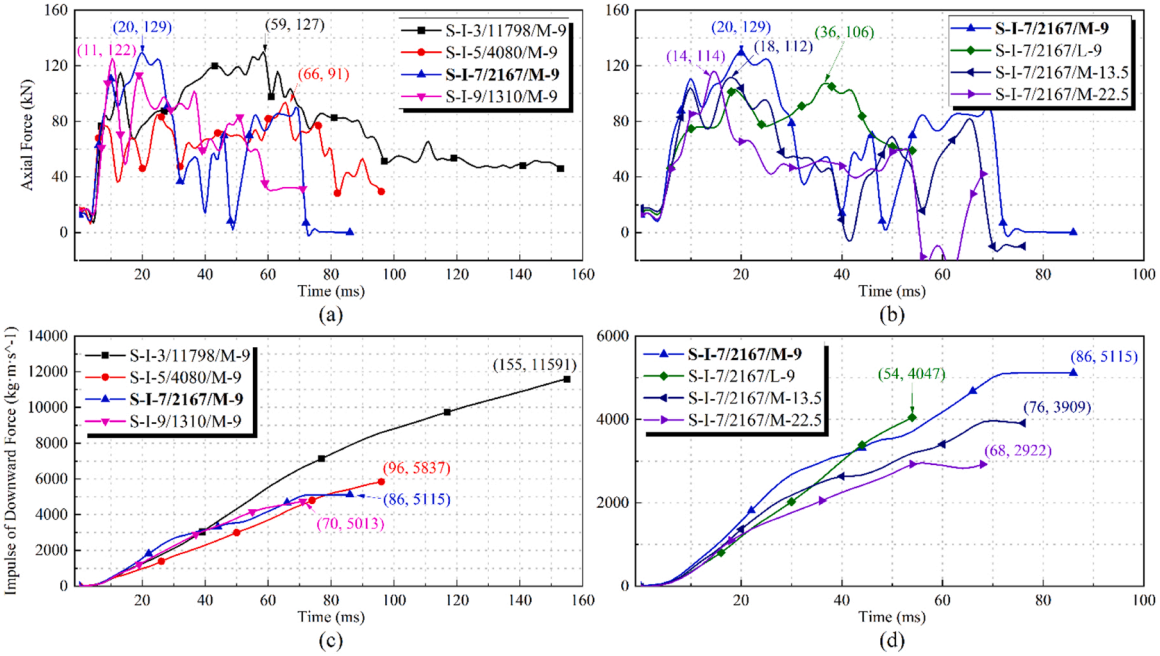

Fig. 21. Downward force and impulse of downward force.

exhibit comparable impulse histories, with the final impulse around 5300 kg·m·s^{-1}. For models with different impact locations and gravity loads, as shown in Fig. 21d, the impulse curves are nearly identical in the first 20 ms, while then diversifying in some degree. It is also worthnoting that the final impulse of experimental groups in Fig. 21d all lower than the control group, S-I-7/2167/M-9, and this phenomenon demands further investigations.

The parametric study reveals that the progressive collapse of RC frames is a complex process affected by various factors. Nonetheless, it can be conceptually differentiated into two stages. The first one is the impact loading stage, characterised by the rapid summit of CRP displacement and exceedance of CRP acceleration than the gravitational acceleration. The second one is similar to NCR and is therefore called the gravity load stage.Fig. 22.

4. Frame structures under ICR

Progressive collapse is the global performance of structures. To gain a deeper insight into the impact-induced progressive collapse mechanisms, FE simulations are performed on the spatial frame level. In order to exclude the influence of lateral stiffness, scenarios were also simulated where the lateral displacement of the structure is constrained. The example spatial frame model [7] consists of a three-storey reinforced concrete frame with two spans in X-axis directions, with a floor height of 3 m. The longer (X-axis) and shorter (Y-axis) spans are 6 m and 3 m, respectively. The concrete compressive strength is 24 MPa, with a density of 2500 kg/m^3 , in the employed CSCM model. The yield strength for longitudinal rebars and stirrups are 335 MPa and 235 MPa, respectively. The *LOAD_NODE_SET keyword is employed to apply uniformly distributed loads, which are 4 kN/m^2 and 19.2 kN/m^2 for the slab and beams, respectively. Other parameters were remained consistent with previous models.

4.1. Frame structures

Fig. 23 presents the vertical displacement history at CRP. The verified model shows minor discrepancies from the example model during the descending phase. However, the differences in residual displacement were minimal, both being around 225 mm. The vertical displacement of the CRP in the ICR model reached 590 mm (F-I-10/2167/M-72). This indicates that frames are more severely damaged under ICR. Nonetheless, progressive collapse is still prevented in the ICR model because the load is within the load-bearing capacity of remaining slabs and columns.

When the load on beams and slabs for the NCR frame increased to 100 kN/m^2, corresponding to F-N-NA-88.2, the displacement reached 350 mm without experiencing progressive collapse. In contrast, the corresponding ICR frame, F-I-10/2167/M-88.2, exhibits a toppling-style progressive collapse (Fig. 24). While the frame did not attain the collapse state immediately after impact, its diminished resistance led to ongoing deformation. In the damage development stage, the P-Δ effect began to manifest, and the frame inclined to one side. The frame entered the collapse stage rapidly ranging from 8.5 s to 10 s. Subsequently, the

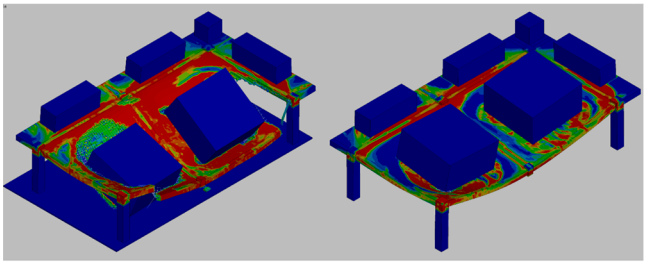

Fig. 22. Damage contours of S-I-7/2167/M-22.5 (ICR, the left) and S-N-NA-22.5 (NCR, the right).

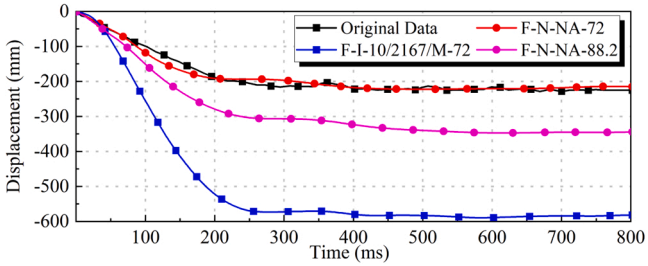

Fig. 23. History comparison of vertical displacement at CRP.

second and third floors collapsed and impacted the first floor and rigid ground.

4.2. Frame structures with boundary constraints

The presented models in the Section 4.2 are characterised with weak lateral stiffness. The lateral stiffness of actual structures is provided by multi-spans in which the resistance against progressive collapse will be governed by beams that prevent the occurrence of toppling-style collapse. In this section, rigid lateral constraints were applied to beam-column joints on each floor, ensuring the collapse resistance of the frame depends solely on the horizontal load-bearing members.

The CRP displacement was significantly reduced after imposing lateral constraints. Compared to F-N-NA-72 and F-I-10/2167/M-72, the residual vertical displacement decreased from 225 mm to 93 mm for FBC-N-NA-72 and from 590 mm to 298 mm for FBC-I-10/2167/M-72. Evidently, the presence of lateral constraints fully utilises the CA. Fig. 25 compares the displacement contour of the frames with boundary constraints under the two removal approaches. It can be observed that after ICR, the displacement of CRPs at each floor is larger than those in the NCR case, indicating the presence of downward forces. The vertical displacement of the CRP on the first floor after ICR is 298 mm, while the displacement on the second and third floors was nearly identical at 271 mm. In the NCR case, the vertical displacement of CRP on the first to third floors were 93 mm, 87 mm, and 87 mm, respectively. Fig. 25c displays the displacement contour of FBC-I-10/2167/M-9 before collapse. It can be observed that the model exhibits a decreasing trend of displacement from the first to the third floor. Progressive collapse is triggered by the longitudinal rebar fracture of the beams on the first floor. As the first floor failed, the load previously borne by the constrained corner columns of the first floor needs to be transferred by the second and third floors, which is beyond their capacity. Therefore, the failure of the first floor ultimately led to the progressive collapse of the frame (Fig. 25d).

5. Design considering ICR

The progressive collapse performance of RC frame structures under ICR is affected by various factors while ignoring ICR will lead to non-conservative results. Based on this finding, following recommendations are proposed to facilitate the progressive collapse design considering ICR:

1. The behaviour of RC frames subjected to ICR is featured with two stages: the impact loading stage and the gravity load stage. In the impact loading stage, the downward force induced by the impacted column played a predominant role in the progressive collapse behaviour of structures. In this stage, impact scenarios and column parameters should be considered in the progressive collapse design. The duration of column removal is related to impact scenarios and the column's resistance against impact, which may potentially inflict damage upon structural members adjacent to the impacted column.

2. Structural behaviour during the gravity load stage resembles event-independent behaviour that existing resistance mechanisms are

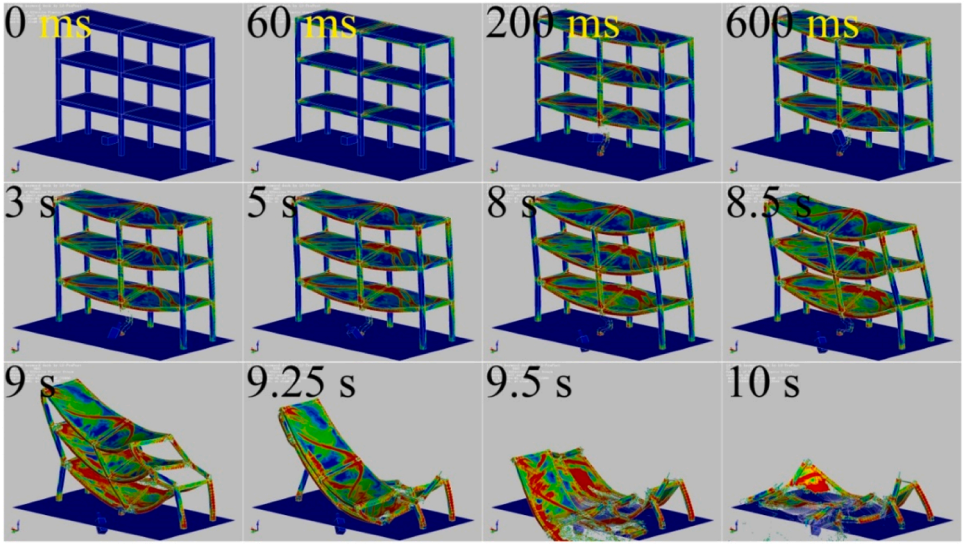

Fig. 24. Collapse course of the example frame subjected to ICR (F-I-10/2167/M-88.2).

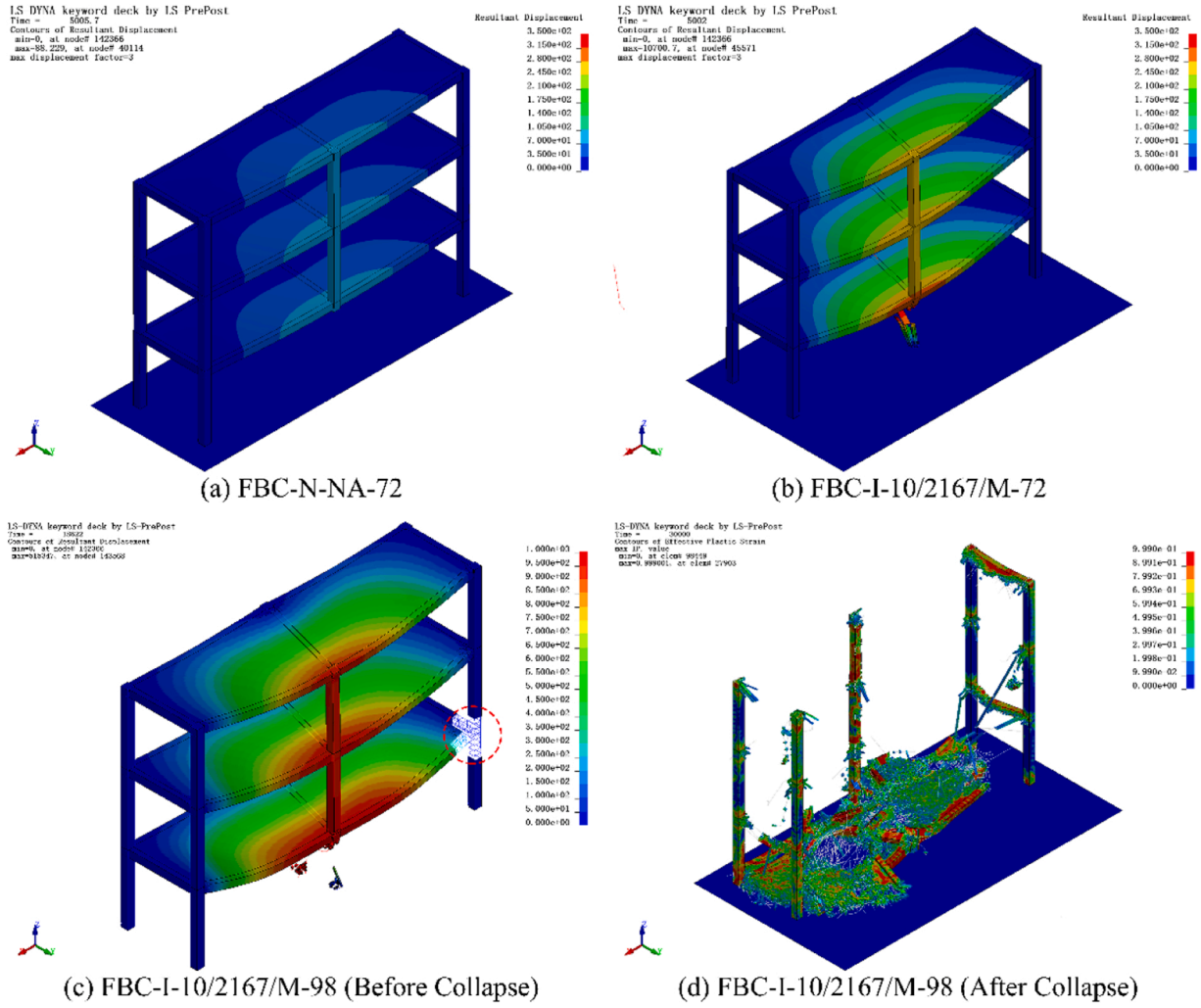

Fig. 25. Displacement contour.

applicable with modifications of downward forces and initial damage. However, it is recommended to only consider the resistance provided by CA since the short-duration-high-magnitude downward force could cause the snap-through effect under ICR.

3. Impact column removal is a low-probability event, so it is evidently uneconomical to design all structural members resisting both

impact and progressive collapse. Therefore, partition strategies implemented in relevant specifications [50] can be employed when performing progressive collapse design considering ICR. Specifically, structural members can be differentiated as controlled public access and uncontrolled public access. For uncontrolled public access members, consideration must be given to ICR in their progressive collapse design.

4. The downward force function till rebars connecting columns and superstructures fracture. Therefore, for progressive collapse design of RC structures, simply increasing the connecting rebars at the intersection of columns and superstructures does not necessarily lead to beneficial outcomes. A rational design considering ICR should guarantee that connections between impacted columns and superstructures do not transfer excessive downward force against the resistance mechanisms of structures during lateral impact.

6. Conclusions

In this paper, progressive collapse performances of RC frame structures subjected to impact column removal (ICR) are studied utilizing LS-DYNA, in which validations were conducted on the column, substructure, and frame levels, respectively. In the modelling process, a valuing methodology is proposed to quantitatively consider the influence of element size on the ERODE parameter.

It is revealed that the impact loading induces a downward force on the superstructure, subsequently leading to a snap-through effect in progressive collapse behaviour. Consequently, only the CA could be mobilised for two-span beams. Besides, the impact loading causes initial damage to structures. Consequently, RC frames subjected to ICR face a higher risk of progressive collapse. Specific conclusions are as follows:

1. Due to the influence of the downward force, damage in the substructure under ICR surpasses that under NCR. Furthermore, the impact loading also leads to circular damage areas on the RC slab, weakening the tensile membrane action of the substructure. According to resistance mechanisms, the substructure under ICR directly falls into the CA. The CRP displacement peak for the substructure under ICR, which occurs when the column fails during impact loading, is approximately five times that of NCR.
2. Parameter analysis reveals that various factors affect the progressive collapse performance of RC frames under ICR. The vertical displacement peak is positively correlated with the impact velocity. The progressive collapse resulting from ICR can be classified into two stages: the impact loading stage, characterised by significant downward force, and the gravity load stage, resembling the scenario under NCR, where the impact loading may still exhibit minor influence by initial damage.
3. Despite no apparent pattern being observed on the shape pattern of downward force curves, it is summarised that the peak value of the downward force is around 100 kN regardless of variable changes. The shape of downward force curves is featured with the two-peaks pattern in most cases but is also influenced by specific failure scenarios. Nevertheless, the impulse of downward force curves manifests stability, with comparable final impulses around 5300 $kg{\cdot}m{\cdot}s^{-1}$. Further investigations are still necessary on their formularised quantifications.
4. ICR and NCR may lead to different progressive collapse results. The ICR substructure failed to sustain progressive collapse under 2.5 times the nominal loads, while the NCR substructure remained intact, which indicates that the downward force and the initial damage elevate the risk of progressive collapse.
5. Adverse influences are also observed on frame structures subjected to ICR. Frames with relatively low lateral stiffness could exhibit a toppling-style progressive collapse after ICR. Therefore, it is necessary to consider the influence of lateral stiffness when substituting partial frames for complete frames in progressive collapse studies.
6. Substructure and frame models precluding the influence of lateral stiffness demonstrate similarities on progressive collapse performances. Frames employing ICR may result in progressive collapse at a relatively low load level. Concrete damage intensifies progressively from the top downward in the ICR frame, forming a penetrating diagonal damage zone at the first floor similar to slabs in substructures, which diminishes the tensile membrane action of the frame.

Declaration of Generative AI and AI-assisted technologies in the writing process

During the preparation of this work, the author used ChatGPT 3.5 in order to check whether one specific noun countable or non-countable, for example, ‘force’, ‘analysis’, ‘authenticity’, etc. After using this tool, the author reviewed and edited the content as needed and takes full responsibility for the content of the publication.

CRediT authorship contribution statement

Fan Yi: Writing – review & editing, Writing – original draft, Validation. **Wei-Jian Yi:** Writing – review & editing, Supervision, Project administration, Conceptualization. **Jing-Ming Sun:** Writing – review & editing, Data curation. **Jia Ni:** Validation. **Qing-Feng He:** Investigation. **Yun Zhou:** Investigation, Funding acquisition.

Declaration of Competing Interest

The authors declared that they have no conflicts of interest to this work.

Data Availability

Data will be made available on request.

Acknowledgement

The authors sincerely appreciate the funding support provided by the National Natural Science Foundation of China (NSFC) (No.51878264) and the National Natural Science Foundation of China (NSFC) (No.52278306).

References

[1] Yi W-J, He Q-F, Xiao Y, et al. Experimental study on progressive collapse-resistant behavior of reinforced concrete frame structures. Acids Struct J 2008;105(4):433.
[2] Qian K, Li B. Slab effects on response of reinforced concrete substructures after loss of corner column. Acids Struct J 2012.
[3] Izzuddin BA, Vlassis AG, Elghazouli AY, et al. Progressive collapse of multi-storey buildings due to sudden column loss - Part I: Simplified assessment framework. Eng Struct 2008;30(5):1308–18.
[4] Yu J, Tan K-H. Experimental and numerical investigation on progressive collapse resistance of reinforced concrete beam column sub-assemblages. Eng Struct 2013; 55:90–106.
[5] Bao Y, Kunnath SK, El-Tawil S, et al. Macromodel-based simulation of progressive collapse: RC frame structures. J Struct Eng 2008;134(7):1079–91.
[6] Adam JM, Parisi F, Sagaseta J, et al. Research and practice on progressive collapse and robustness of building structures in the 21st century. Eng Struct 2018;173: 122–49.
[7] Shi Y, Li Z-X, Hao H. A new method for progressive collapse analysis of RC frames under blast loading. Eng Struct 2010;32(6):1691–703.
[8] Li Z, Liu Y, Huo J, et al. Experimental assessment of fire-exposed RC beam-column connections with varying reinforcement development lengths subjected to column removal. Fire Saf J 2018;99:38–48.
[9] Li Y, Lu X, Guan H, et al. A case study on a fire-induced collapse accident of a reinforced concrete frame-supported masonry structure. Fire Technol 2016;52(3): 707–29.
[10] Gombeda MJ, Naito CJ, Quiel SE, et al. Blast-induced damage mapping framework for use in threat-dependent progressive collapse assessment of building frames. J Perform Constr Facil 2017;31(2):04016089.
[11] Zhang CW, Gholipour G, Mousavi AA. Nonlinear dynamic behavior of simply-supported RC beams subjected to combined impact-blast loading. Eng Struct 2019; 181:124–42.

[12] Gholipour G, Zhang C, Mousavi AA. Numerical analysis of axially loaded RC columns subjected to the combination of impact and blast loads. Eng Struct 2020; 219:110924.
[13] Kang H, Kim J. Progressive collapse of steel moment frames subjected to vehicle impact. J Perform Constr Facil 2015;29(6):04014172.
[14] Sezen H., Center P.E.E.R. Structural Engineering Reconnaissance of the August 17, 1999 Earthquake: Kocaeli (Izmit), Turkey. Pacific Earthquake Engineering Research Center, 2000,
[15] Symonds PS, Mentel TJ. Impulsive loading of plastic beams with axial constraints. J Mech Phys Solids 1958;6(3):186–202.
[16] Demartino C, Wu J, Xiao Y. Experimental and numerical study on the behavior of circular RC columns under impact loading. Procedia Eng 2017;199:2457–62.
[17] Chen L, Wu H, Fang Q, et al. Full-scale experimental study of a reinforced concrete bridge pier under truck collision. J Bridge Eng 2021;26(8):05021008.
[18] Li RW, Zhou DY, Wu H. Experimental and numerical study on impact resistance of RC bridge piers under lateral impact loading. Eng Fail Anal 2020;109.
[19] Louw J, Maritz G, Loedolff MJ. The behaviour of RC columns under impact loading. J Civ Eng 1992;1992(11):371–8.
[20] Sha YY, Hao H. Laboratory tests and numerical simulations of CFRP strengthened RC pier subjected to barge impact load. Int J Struct Stab Dyn 2015;15(2).
[21] Feyerabend M. Hard transverse impacts on steel beams and reinforced concrete beams [Ph. D. thesis]: [Doctor]. Germany: University of Karlsruhe, 1988.
[22] Fan W, Liu B, Consolazio GR. Residual capacity of axially loaded circular RC columns after lateral low-velocity impact. J Struct Eng 2019;145(6):04019039.
[23] Cai J, Ye J-B, Chen Q-J, et al. Dynamic behaviour of axially-loaded RC columns under horizontal impact loading. Eng Struct 2018;168:684–97.
[24] Qian K, Li B. Dynamic and residual behavior of reinforced concrete floors following instantaneous removal of a column. Eng Struct 2017;148:175–84.
[25] Qian K, Wang D-F, Huang T, et al. Initial damage and residual behavior of RC beam-slab structures following sudden column removal-numerical study. Structures 2022;36:650–64.
[26] Qian K, Chen XY, Huang T. Dynamic response of RC beam-slab substructures following instantaneous removal of columns. J Build Eng 2022;45.
[27] Thilakarathna HMI, Thambiratnam DP, Dhanasekar M, et al. Numerical simulation of axially loaded concrete columns under transverse impact and vulnerability assessment. Int J Impact Eng 2010;37(11):1100–12.
[28] Kishi N, Khasraghy SG, Kon-No H. Numerical simulation of reinforced concrete beams under consecutive impact loading. Acids Struct J 2011;108(4).
[29] Sha Y, Hao H. Laboratory tests and numerical simulations of barge impact on circular reinforced concrete piers. Eng Struct 2013;46:593–605.
[30] Fan W, Shen D, Yang T, et al. Experimental and numerical study on low-velocity lateral impact behaviors of RC, UHPFRC and UHPFRC-strengthened columns. Eng Struct 2019;191:509–25.
[31] Li HW, Chen WS, Pham TM, et al. Analytical and numerical studies on impact force profile of RC beam under drop weight impact. Int J Impact Eng 2021;147.
[32] Li J, Hao H. Numerical study of structural progressive collapse using substructure technique. Eng Struct 2013;52:101–13.
[33] Pham AT, Tan KH, Yu J. Numerical investigations on static and dynamic responses of reinforced concrete sub-assemblages under progressive collapse. Eng Struct 2017;149:2–20.
[34] Yu J, Luo LZ, Li Y. Numerical study of progressive collapse resistance of RC beam-slab substructures under perimeter column removal scenarios. Eng Struct 2018; 159:14–27.
[35] Qian K, Liang S-L, Feng D-C, et al. Experimental and numerical investigation on progressive collapse resistance of post-tensioned precast concrete beam-column subassemblages. J Struct Eng 2020;146(9):04020170.
[36] Liu B, Fan W, Guo W, et al. Experimental investigation and improved FE modeling of axially-loaded circular RC columns under lateral impact loading. Eng Struct 2017;152:619–42.
[37] Xu X. Performance based approach for loading and design of bridge piers impacted by medium weight trucks. City Coll N Y 2017.
[38] Jiang H, Zhao J. Calibration of the continuous surface cap model for concrete. Finite Elem Anal Des 2015;97:1–19.
[39] Xu S, Wu P, Liu Z, et al. Calibration of CSCM model for numerical modeling of UHPCFTWST columns against monotonic lateral loading. Eng Struct 2021;240: 112396.
[40] He Y, Fan W. Plastic-damage cap model with crack closure behavior for concrete modeling. J Eng Mech 2022;148(11).
[41] Standard Test Method for Compressive Strength of Cylindrical Concrete Specimens ASTM International West Conshohocken.
[42] Gopalaratnam V, Shah SP. Softening response of plain concrete in direct tension. : J Proc 1985:310–23.
[43] Gu Z-H, Zhang X-Q. Experimental Investigation of Complete Stress-Deformation Curves of Concrete in Tension. ISSN 1000-6869 in Chinese J Build Struct 1988;9 (4):45–53.
[44] Ross CA, Tedesco JW, Kuennen ST. Effects of strain rate on concrete strength. Mater J 1995;92(1):37–47.
[45] Fan W, Xu X, Zhang Z, et al. Performance and sensitivity analysis of UHPFRC-strengthened bridge columns subjected to vehicle collisions. Eng Struct 2018;173: 251–68.
[46] Sun J-M, Yi W-J, Chen H, et al. Dynamic responses of RC columns under axial load and lateral impact. J Struct Eng 2023;149(1):04022210.
[47] Yu J, Luo L-z, Fang Q. Structure behavior of reinforced concrete beam-slab assemblies subjected to perimeter middle column removal scenario. Eng Struct 2020;208:110336.
[48] GB 50009-2012 Load Code for the Design of Building Structures. China Building Industry Press Beijing, China, 2012.
[49] AASHTO LRFD Bridge Design Specifications 8th edition. Washington, D.C. American Association of State Highway and Transportation Officials, 2017.
[50] GSA, Alternate path analysis & design guidelines for progressive collapse resistance. GSA Washington, DC, 2013.